JOURNAL OF PETROLOGY

Journal of Petrology, 2020, Vol. 61, No. 4: egaa043
doi: 10.1093/petrology/egaa043
Advance Access Publication Date: 26 March 2020
Original Article

OXFORD

High-pressure Cu–Fe–S Phase Equilibria: some Experimental and Thermodynamic Constraints on Sulfides in Subduction Zones and the Lithospheric Mantle

Julie L. Brown [1]*, Sabastien C. Dyer[2], James E. Mungall[3], Andrew G. Christy[4,5] and David J. Ellis[6]

[1]Canadian Nuclear Safety Commission, Ottawa ON, K1P 5S9, Canada; [2]Department of Earth Sciences, University of Toronto, Toronto, ON M5S 3B1, Canada; [3]Department of Earth Sciences, Carleton University, Ottawa, ON K1S 5B6, Canada; [4]School of Earth and Environmental Sciences, University of Queensland, Brisbane, QLD 4072, Australia; [5]Geosciences, The Queensland Museum, 122 Gerler Road, Hendra, QLD 4011, Australia; [6]Research School of Earth Sciences, Australian National University, Canberra, ACT 0200, Australia

*Corresponding author. Telephone: +1 (613) 944-1984. Fax: +1 (613) 947-4205.
E-mail: julie.brown@canada.ca

Received October 22, 2018; Accepted March 18, 2020

ABSTRACT

High-pressure phase relations for much of the Cu–Fe–S system have not previously been determined experimentally. Experimental studies have concentrated on low-pressure phase relations and cannot explain high-pressure sulfide mineral inclusion assemblages in some natural blueschists and eclogites. In particular, the coexistence of pyrite + covellite at 1·0 GPa, and pyrite + bornite at 1·9 GPa, observed in New Caledonian rocks, is precluded by tie-lines between S and bornite, and S and the intermediate solid solution (*iss*), in the published low-pressure experimental topologies at corresponding temperatures. In addition, the Cu content (up to ~10 at%) of pyrrhotite in eclogite exceeds the experimentally determined maximum for Cu in solid solution with pyrrhotite at low pressures and at corresponding temperatures. We have performed six experiments in which natural chalcopyrite starting material was equilibrated at conditions ranging from 1·0 to 1·7 GPa and 500 to 650 °C. At 1 GPa chalcopyrite is replaced by *iss*. The *iss* phase undergoes a terminal breakdown reaction between 1·0 and 1·7 GPa, being replaced by a new assemblage of bornite, pyrite, and pyrrhotite. Our experimental results confirm predictions from the SUPCRT thermodynamic database (Johnson *et al.*, 1992; *Computers & Geosciences* **18**, 899–947) but not that of Robie & Hemingway (1995; *US Geological Survey Bulletin* **2131**). The former database is therefore recommended for calculation of high-pressure sulfide phase relations. Chalcopyrite and its high-temperature, low-f_{S_2} equivalent, *iss* are not stable at pressures corresponding to much of blueschist–eclogite-facies metamorphism. These results are also applicable to sulfide assemblages in the lithospheric mantle along both oceanic and continental geotherms; the subsolidus Cu-rich mineral in the lithosphere at depths of 30 to >65 km must be bornite–digenite solid solution (bn-*ss*) rather than *iss* as is commonly assumed.

Key words: Cu–Fe–S phase equilibria; high pressure; sulfide experiments

INTRODUCTION

High-pressure phase relations for the Cu–Fe–S system have not previously been determined experimentally, although numerous previous experimental or modelling studies and reviews have concentrated on low-pressure phase relations (Merwin & Lombard, 1937;

Roseboom & Kullerud, 1958; Kullerud & Yoder, 1959; Morimoto & Kullerud, 1963; Kullerud, 1964; Toulmin & Barton, 1964; Morimoto & Kullerud, 1966; Yund & Kullerud, 1966; Roseboom, 1966; Cabri & Hall, 1972; Barton, 1973; Schneeberg, 1973; Craig & Scott, 1974; Potter & Evans, 1976; Sugaki *et al.*, 1981; Kojima & Sugaki, 1985; Vaughan & Craig, 1997; Grguric *et al.*, 2000; Seal *et al.*, 2001; Lusk & Bray, 2002). Brown *et al.* (2014) documented sulfide mineral inclusion assemblages in lawsonite and garnet from the New Caledonian high-pressure metamorphic belt, summarized in Fig. 1 and in Table 1. Some key observations from that study include the following:

1. prograde pyrite + covellite inclusions were trapped within lawsonite in lawsonite blueschist at 1·0 GPa;
2. covellite was not seen in inclusions trapped at pressures and temperatures above 1·5 GPa, 500 °C;
3. pyrrhotite is stable at 1·5 GPa, 500 °C and dominates assemblages in the omphacite mineral zone from 1·5 to 1·7 GPa, and from 550 to 580 °C; pyrrhotite in metabasaltic rocks is Cu-rich;
4. the highest-pressure (1·9 GPa, >600 °C) prograde sulfide assemblages, found trapped as inclusions within almandine garnet, are characterized by the coexistence of pyrite and bornite.

The differences between observations of sulfide inclusions documented by Brown *et al.* (2014) and the existing experimental literature for Cu–Fe sulfides at low pressure (Fig. 2) informed the design of experiments and calculations of phase equilibria presented in this paper. For instance, the observed coexistence of pyrite + covellite within inclusions that were trapped in lawsonite that crystallized and equilibrated at 1·0 GPa, and of pyrite + bornite inclusions trapped within garnet

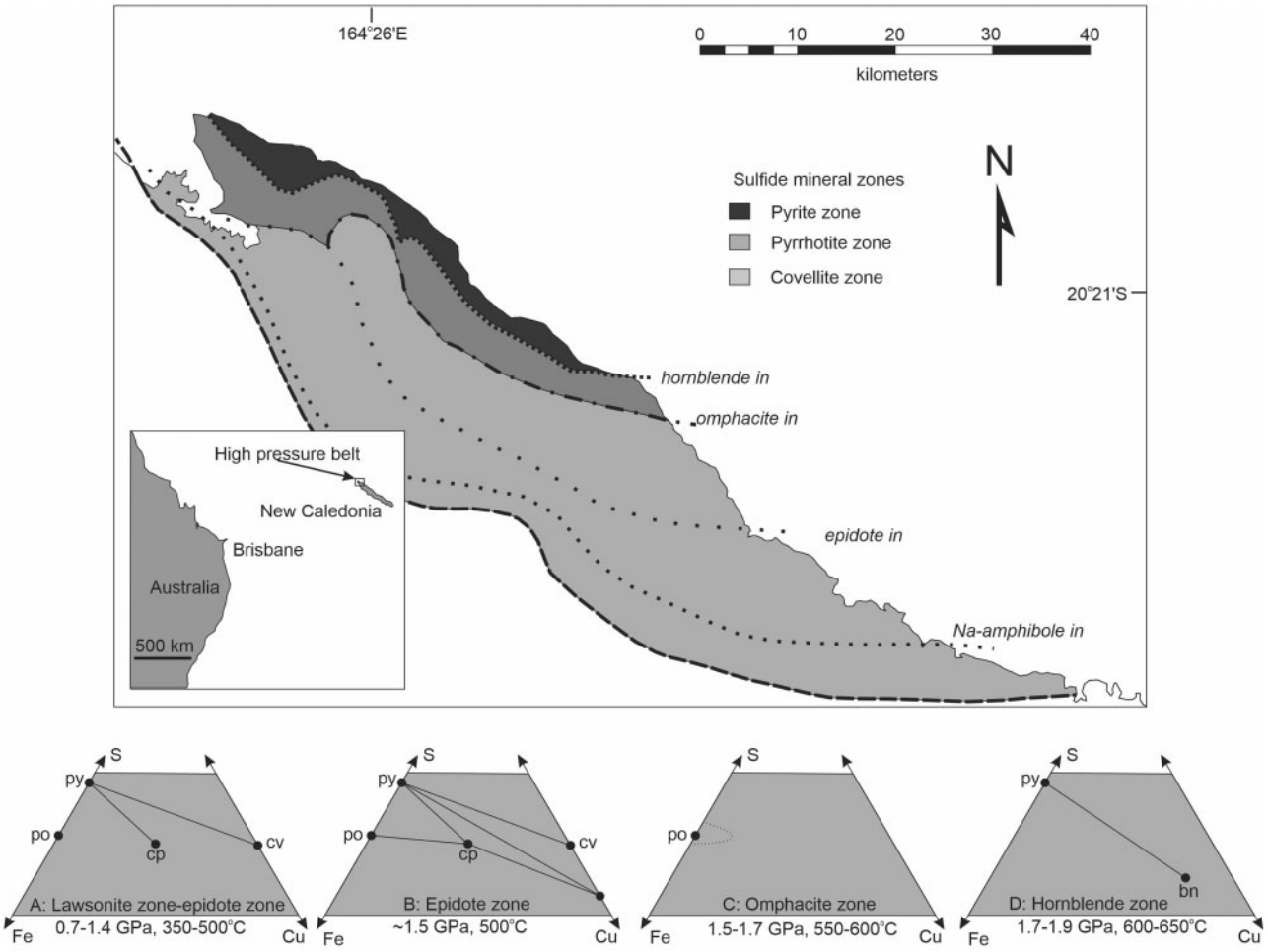

Fig. 1. Location map of the high-pressure belt in northern New Caledonia showing the positions of silicate isograds and sulfide zones, where metamorphic grade increases to the NW. Below the map, the observed sulfide mineral coexistences in the Cu–Fe–S system that characterize the high-pressure belt are summarized in (a)–(d), described fully by Brown *et al.* (2014). Prograde covellite inclusions were found within the lawsonite and epidote zones (a, b), and were not found above 1·5 GPa, 500 °C (c–d). Pyrrhotite dominates assemblages in the omphacite zone, and is copper-rich in metabasaltic rocks, as shown by the dotted line in (c). In the highest-pressure portion of the belt, inclusions in almandine garnet are characterized by the coexistence of bornite and pyrite (d). po, pyrrhotite; py, pyrite; cp, chalcopyrite; cv, covellite; bn, bornite. *P–T* estimates for silicate metamorphic zones are from Carson *et al.* (1999) and Fitzherbert *et al.* (2003).

Table 1: Summary of dominant prograde sulfide mineralogy, New Caledonia (Brown *et al.*, 2014)

Metamorphic zone (silicate)	Sulfide inclusions in prograde lawsonite and garnet	Sulfide mineral zone
Lawsonite zone; 1·0 GPa, 400 °C	Chalcopyrite, pyrite, and covellite in lawsonite and pyrite–chalcopyrite in garnet (pyrrhotite absent)	Covellite
Epidote zone; 1·4–1·5 GPa, <500 °C	Covellite, pyrite, digenite, and pyrrhotite in garnet	Covellite
Omphacite zone; 1·5–1·7 GPa, 550–580 °C	Dominantly pyrrhotite, with high Cu content in pyrrhotite in meta-basalt (covellite absent) in garnet	Pyrrhotite
Hornblende zone; 1·9 GPa, 600–620 °C	Pyrite and bornite (pyrrhotite absent) in garnet	Pyrite

P–T estimates for silicate metamorphic zones from Carson *et al.* (1999) and Fitzherbert *et al.* (2003).

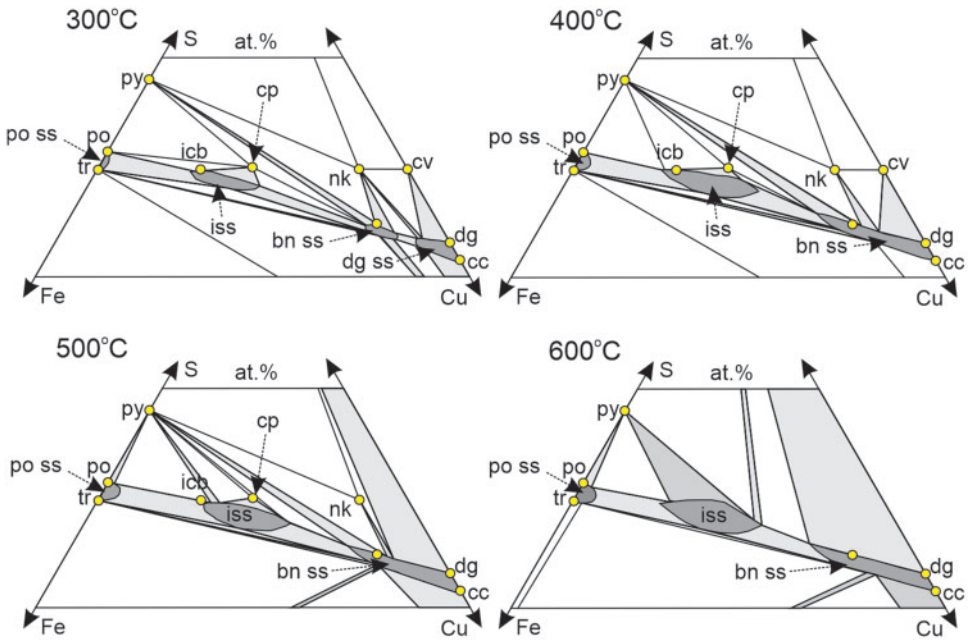

Fig. 2. Compositions and chemography of possible phases in the Cu–Fe–S system based on low-pressure experimental petrology. Yellow circles are ideal stoichiometric phases, connected by continuous black tie-lines. Solid solution fields are indicated with dark shading, joined to other phases by light grey two-phase fields. Data sources are summarized in the text.

that formed at 1·9 GPa, are precluded in the respective low-pressure experimental topologies for these phases at the inferred temperatures, owing to tie-lines between S and bornite, and between S and the intermediate solid solution (*iss*) (Figs 1 and 2). In addition, the bulk Cu content (up to ∼10 at%) of sulfide mineral intergrowths interpreted to represent breakdown products of high-pressure pyrrhotite from the omphacite zone, as determined by bulk area scans (Brown *et al.*, 2014), exceeds the experimentally determined maximum for Cu in solid solution with pyrrhotite at low pressures (∼3·5 at%; Kullerud, 1964; Mungall *et al.*, 2005). A general observation from Brown *et al.* (2014) is that the sulfide inclusions are predominantly Cu and Fe sulfides, with Cu content increasing with metamorphic grade. Rather than chalcopyrite, the most common Cu–Fe sulfide at the Earth's surface, bornite was observed in the highest-pressure mineral inclusions in New Caledonia—so we focused our experimental work and thermodynamic analysis on investigating this phenomenon.

In this paper, we present new high-pressure experimental data and interpret the change in phase diagram topology for Cu–Fe–S assemblages during subduction-zone metamorphism as deduced from petrography (presented by Brown *et al.*, 2014) and thermodynamic calculations (presented in this paper). To this end, natural chalcopyrite starting material was equilibrated at conditions spanning those under which the breakdown of chalcopyrite or *iss* was inferred to have occurred in the natural assemblages. The results are compared with thermodynamic predictions of phase equilibria in the system Cu–Fe–S. We explore the expected stability of key Fe sulfide and Cu–Fe sulfide assemblages as a function of pressure. Where thermodynamic data exist, low-*P* (atmospheric) experimental phase equilibria are extrapolated to higher pressure, with the objective of elucidating mineral paragenesis and phase relations.

Table 2: Stoichiometric composition and crystallography of some sulfide minerals

Mineral	Abbreviation	Composition	Crystal structure	Thermal stability (°C) at ~1 bar	Reference
Covellite	Cv	CuS	Hexagonal	<507	Roseboom & Kullerud, 1958
Chalcocite	Cc	Cu_2S	<100 °C monoclinic; 100–435 °C hexagonal; >435 °C cubic	1129	Morimoto & Kullerud, 1963; Roseboom, 1966; Potter & Evans, 1976
High digenite	Dg	$(Cu,Fe)_9S_5$	Cubic	77–1129	Morimoto & Kullerud, 1963
Bornite	Bn	Cu_5FeS_4	<228 °C tetragonal; >228 °C cubic	1100	Morimoto & Kullerud, 1966
Chalcopyrite	Cp	$CuFeS_2$	Tetragonal	557	Cabri & Hall, 1972; Barton, 1973
Cubanite	Cb	$CuFe_2S_3$	<213 °C orthorhombic; >213 °C tetragonal	<~200	Cabri, 1973
Isocubanite	Icb	$CuFe_2S_3$	Cubic	>~200	Caye *et al.*, 1988
Intermediate solid solution	Iss	$(Cu,Fe)_{1+x}S$	Cubic	>~200	
Nukundamite	Nk	$Cu_{3.38}Fe_{0.62}S_4$	Hexagonal–rhombohedral	224–501	Merwin & Lombard, 1937; Inan & Einaudi, 2002
Troilite	Tr	FeS	Hexagonal	1190	Kullerud & Yoder, 1959
Pyrrhotite	Po	Fe_7S_8	<300 °C monoclinic; >300 °C hexagonal	1190	Kullerud & Yoder, 1959; Toulmin & Barton, 1964
Pyrite	Py	FeS_2	Cubic	743	Kullerud & Yoder, 1959
Villamaninite	Vi	CuS_2	Cubic (pyrite structure type)	—	Bayliss, 1989; Marcos *et al.*, 1996

Table 3: Reactions in the Cu–Fe–S system

Number	Reaction name	Reaction	Reaction ΔV_{solid} (J bar^{-1})	Variance
1	py = po	$FeS_2 = FeS + 0{\cdot}5S_2$	−0·574	Univariant (degenerate)
2	cp = py + bn	$5CuFeS_2 + S_2 = 4FeS_2 + Cu_5FeS_4$	−2·511	Univariant
3	cp = po + bn	$5CuFeS_2 = 4FeS + Cu_5FeS_4 + S_2$	−4·807	Univariant
4	cv = cc	$2CuS = Cu_2S + 0{\cdot}5S_2$	−1·336	Univariant (degenerate)
5	cp = po + py + bn	$5CuFeS_2 = 2FeS + 2FeS_2 + Cu_5FeS_4$	−3·659	Univariant
6a	bn = cc + po + py	$2Cu_5FeS_4 = 5Cu_2S + FeS + FeS_2$	−1·729	Univariant
6b	bn = dg + po + py	$2Cu_5FeS_4 = 1{\cdot}39Cu_{7.2}S_4 + FeS + FeS_2$	−1·729	Univariant
7	po + cp = py + bn	$FeS + 5CuFeS_2 + 1{\cdot}5S_2 = 5FeS_2 + Cu_5FeS_4$	−1·932	Invariant
8	po + icb = py + bn	$FeS + 5CuFe_2S_3 + 4S_2 = 10FeS_2 + Cu_5FeS_4$	−1·562	Invariant
9	nk = cv + py	$Cu_{5.5}FeS_{6.5} + 0{\cdot}5S_2 = 5{\cdot}5CuS + FeS_2$	+5·268	Univariant
10	cv + bn = nk + dg	$10CuS + 2Cu_5FeS_4 = 2Cu_{5.5}FeS_{6.5} + Cu_9S_5$	−20·89	Univariant
11	nk + bn = py + dg	$7Cu_{5.5}FeS_{6.5} + 13Cu_5FeS_4 = 20FeS_2 + 11{\cdot}5Cu_9S_5$	−109·49	Univariant
12	nk = py + cv + dg	$4Cu_{5.5}FeS_{6.5} = 4FeS_2 + 13CuS + Cu_9S_5$	+5·257	Inivariant
13a	nk + cv = *bnss*	$Cu_{3.38}Fe_{0.62}S_4 + CuS = Cu_{4.395}Fe0.6S_{3.175} + 0{\cdot}91S_2$	−3·527	Univariant
13b	nk + py = bn	$1{\cdot}47Cu_{3.38}Fe_{0.62}S_4 + 0{\cdot}12FeS_2 = 0{\cdot}62Cu_5FeS_4 + 1{\cdot}062S_2$	−3·06	Univariant
14a	nk = py + bn	$Cu_{3.38}Fe_{0.62}S_4 = 0{\cdot}136FeS_2 + 0{\cdot}773Cu_{4.395}Fe0.6S_{3.175} + 0{\cdot}637S_2$	−2·748	Univariant
14a	nk = bn + cv	$Cu_{3.38}Fe_{0.62}S_4 = 0{\cdot}62Cu_5FeS_4 + 0{\cdot}28CuS + 0{\cdot}622S_2$	−1·781	Univariant
15	cv = dg	$7{\cdot}2CuS = Cu_{7.2}S_4 + 1{\cdot}6S_2$	−4·157	Univariant
16a	nk = py + cv + bn	$Cu_{3.38}Fe_{0.62}S_4 = 0{\cdot}413FeS_2 + 2{\cdot}345CuS + 0{\cdot}207Cu_5FeS_4$	−0·645	Invariant
16b	nk = py + cv + dg	$Cu_{3.38}Fe_{0.62}S_4 = 0{\cdot}62FeS_2 + 1{\cdot}985CuS + 0{\cdot}194Cu_{7.2}S_4$	−0·900	Invariant
17	py + cv = bn	$FeS_2 + 5CuS = Cu_5FeS_4 + 3{\cdot}5S_2$	−2·731	Univariant

Molar volume data are assessed from Robie & Hemingway (1995).

Relevant end-member sulfide mineral compositions and crystal structures are summarized in Table 2. Theoretical phase equilibria are calculated for the reactions listed in Table 3. The objective of considering these reactions is to assess the stability of these mineral assemblages with increasing pressure and to consider which reactions are likely to replace them at higher pressure.

Whereas at low pressure the most common Cu–Fe sulfide is chalcopyrite (or *iss* at low f_{S_2} or high temperature), we will argue that new sulfide associations are characteristic of the deeper portions of subduction zones and the upper mantle lithosphere.

EXPERIMENTS: HIGH-PRESSURE CHALCOPYRITE STABILITY

Six experiments were conducted in a ¾ inch end-loaded piston cylinder apparatus at the University of Toronto. The starting material was coarse-grained natural chalcopyrite from the former Strathcona Mine, Sudbury. We chose to use natural chalcopyrite because

Table 4: Experimental run conditions and observed phase assemblages

Sample	*T* (°C)	*P* (GPa)	*t* (h)	*iss*	po *ss* (*mss*)	Py	bn	PtS
HPS 01	650	1·7	96	—	x	X	x	—
HPS 02	500	1·0	96	X	x	X	–	—
HPS 03	500	1·7	96	—	x	X	x	—
HPS 04	500	1·2	96	X	x	X	—	—
HPS 05	650	1·0	96	X	x	X	—	x
HPS 06	650	1·2	96	X	x	X	—	x

of our concerns that if we used synthetic chalcopyrite we might inadvertently include other copper sulfide minerals owing to incorrect stoichiometry of reagent mixtures, leading to more ambiguous results if multiple Cu sulfide minerals were observed in run products. The trade-off was that our starting material included traces of a Ni-bearing sulfide, either pyrrhotite or pentlandite, which resulted in the presence of minor quantities of Ni in the product Fe-sulfide phases. Because our aim is to investigate the behaviour of chalcopyrite in natural systems, where Ni is likely to be present, we were not unduly concerned about the added compositional complexity and chose to work with a starting Cu phase known to comprise exactly stoichiometric $CuFeS_2$. The chalcopyrite was hand-picked and then crushed in an agate mortar and pestle under ethanol, dried at 110 °C, and stored in a desiccator until immediately before use. For each experiment the powdered chalcopyrite was loaded into a 5 mm diameter Pt capsule, which was inserted into a MgO sleeve within the hotspot of a cylindrical graphite furnace. The furnace was surrounded by a Pyrex glass sleeve; halite was used as the pressure medium inside a lubricating Pb foil sleeve. The assembly was placed in a WC cylinder and compressed with a ¾ inch WC piston. Pressure was monitored with a Bourdon™ gauge and maintained during heating (i.e. hot piston in method), subject to a 10 % friction correction. Temperature was both measured and controlled using a W–Re thermocouple linked to a Eurotherm™ PID controller. Pressure and temperature are considered accurate within 10 % and 10 °C, respectively. Run conditions are presented in Table 4; all runs were equilibrated for 96 h before quenching by turning off power. The temperature in the charges had dropped to below 100 °C within 1 min of starting the quench.

Analytical methods

Run products were mounted in epoxy and sectioned before examination by reflected light microscopy, scanning electron microscopy (SEM), and electron probe microanalysis (EPMA). EPMA was carried out at the University of Toronto on a JEOL JXA8230 electron microprobe with W filament and five wavelength-dispersive spectrometers. Analyses were conducted with 20 kV accelerating voltage and 50 nA beam current focused to a 1 μm spot. For chalcopyrite, *iss*, and bornite analyses, standards employed were chalcopyrite (Cu, Fe, S), arsenopyrite (As), pentlandite (Ni), cobaltite (Co), sphalerite (Zn), and galena (Pb); for pyrite and pyrrhotite, pyrite was used as the standard for Fe and all others were as listed above.

Experimental results

The phase assemblages observed in all six run products are listed in Table 4. EPMA data for all product phases except cooperite are available as Supplementary Data Electronic Appendix 1; supplementary data are available for downloading at http://www.petrology.oxfordjournals.org.

Only two Cu–Fe-sulfide mineral assemblages were observed in the experimental run products. Figure 3 shows the compositions of all analysed product phases compared with the stoichiometries of end-member sulfide minerals. Representative run products are illustrated in Fig. 4. The contact between the sulfide minerals and the Pt capsule was decorated by a Pt sulfide inferred to be cooperite (PtS) in the two experiments conducted at 650 °C and either 1·0 or 1·2 GPa (Fig. 4a and d). In all other cases the Cu–Fe–S phases were observed to sit in direct contact with the Pt capsule wall. Trace amounts of Pt minerals were observed in some run products, presumably as a result of vapor transport of Pt during the experiments. These grains are too small to analyze by EPMA but they show Pt X-ray emissions so they are either Pt or PtS.

In runs equilibrated at either 1·0 or 1·2 GPa, the chalcopyrite starting material was replaced by *iss* with a composition more Cu-rich and lower in S than the original chalcopyrite (Figs 3a and 4). As commonly observed in quenched experiments (e.g. Yund & Kullerud, 1966; Putnis, 1977), crystals of *iss* contain ubiquitous μm-scale oriented lamellae of an unidentified Cu sulfide that we interpret to have been exsolved in the solid state during the quench. These are visible in Fig. 4 as faint darker grey lines throughout the *iss* grains. Electron probe spots were chosen at random within *iss*; despite this, there is little scatter in the measured *iss* compositions shown in Fig. 3 and we infer therefore that the bulk *iss* composition prior to exsolution during quench was close to the average of these data. In all of the 1·0 and 1·2 GPa runs, a distinctive texture was developed wherein the boundaries between the original chalcopyrite grains were lined with newly grown pyrite (Fig. 4b and d). Irregular masses of pyrrhotite solid solution (po-*ss*) appeared randomly dispersed throughout the *iss* domains (Fig. 4b and d). This phase contains small amounts of Cu and Ni; in Ni-rich magmatic systems it is commonly referred to as monosulfide solid solution (*mss*; e.g. Mungall *et al.*, 2005) but here, we retain the po-*ss* terminology generally used in the Cu–Fe–S literature.

In runs equilibrated at 1·7 GPa, the chalcopyrite was completely replaced by homogeneous bornite–digenite solid solution ('bn-*ss*'; Fig. 4c), within which there were irregular patches of po-*ss*. As in the lower pressure

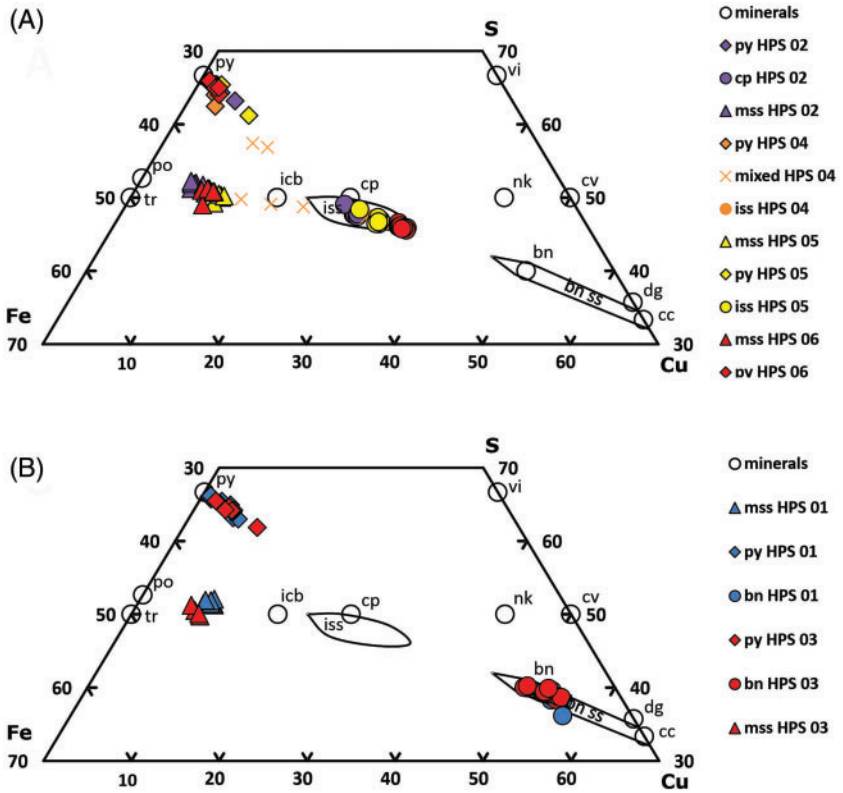

Fig. 3. Run product phase compositions compared with stoichiometric phases and solid solution fields in the Cu–Fe–S system. (a) Phase assemblages at 1·0 and 1·2 GPa. (b) Phase assemblages at 1·7 GPa. cv, covellite, CuS; cc, chalcocite, Cu_2S; dg, digenite, $Cu_{7.2}S_4$; bn, bornite, Cu_5FeS_4; cp, chalcopyrite, $CuFeS_2$; icb, isocubanite, $CuFe_2S_3$; tr, troilite, FeS; po, pyrrhotite, Fe_7S_8; py, pyrite, FeS_2; vi, villamaninite, CuS_2; nk, nukundamite, $Cu_{5.5}FeS_{6.5}$ (or $Cu_{3.9}Fe_{0.6}S_4$); *iss*, intermediate solid solution; bn-*ss*, bornite solid solution. S_2 is an excess fluid component at the *P* and *T* conditions of interest for this study.

runs, pyrite grew along grain boundaries. Between the pyrite and bornite, there was generally a zone of finely intergrown po-*ss* and bn-*ss* (Fig. 4c). The composition of *iss* falls within its solid solution field at 600 °C as determined by Kullerud (1964). The amount of Cu in *iss* is larger at higher temperature. A few analyses from HPS 04 lie along the po-*iss* join or the py-*iss* join, and are interpreted to represent intergrowths so fine that the electron beam impinged on both end-member phases at once. Apart from probable mixed intergrowth compositions, pyrite compositions cluster at a point slightly enriched in Cu and depleted in S relative to stoichiometric FeS_2. In contrast, po-*ss* is notably Cu-rich compared with its usual range in low-pressure environments and is as metal-rich as troilite; the Cu enrichment is most pronounced in the highest-temperature run products. There are trace amounts of Ni in the run products, probably as a result of the accidental incorporation of small amounts of pyrrhotite or pentlandite in the natural chalcopyrite starting material. The most Ni-rich phase is po-*ss*, where Ni concentration never rises above 1·3 wt%; at higher temperatures and pressures where the modal abundance of po-*ss* is greater, the concentration of Ni in this phase falls to less than 0·5 wt%.

The approach to equilibrium needs some attention because reversal experiments were not conducted. We consider the intergrowths of po-*ss* and py to represent phases that were stable together at run conditions, unlike the very fine oriented quench lamellae within *iss*. We are confident that, although textural equilibrium was not attained (Fig. 4), the compositions of our run product phases do reflect equilibrium for several reasons. First, reaction rates and chemical diffusion in base metal sulfide minerals are widely known to be extremely fast. Using self-diffusion coefficients for Fe in pyrrhotite (Condit *et al.*, 1974) and for Cu, Ag in chalcopyrite (Chen & Harvey, 1974), we can estimate diffusivities of base metals in both of these phases to have been approximately $10^{-12}\,m^2\,s^{-1}$ at 650 °C and about $10^{-14}\,m^2\,s^{-1}$ at 300 °C. At these rates, the characteristic diffusive length-scales for volume diffusion [i.e. $(Dt)^{0.5}$ where *D* is the diffusion coefficient and *t* is time] are approximately 300 μm over 24 h at our run conditions and about 2·5 μm at 400 °C over 1 min during quench. The diffusive length-scale exceeds the grain sizes of phases in the experiments and is similar to that of quench phases within *iss*. As the commonly reported exsolution texture in *iss* demonstrates, reaction rates and diffusion are so fast in *iss* that quench phases form and separate in the solid state over times of less than 1 min. Yund & Kullerud (1966) stressed the rapidity of equilibration of iss and bornite at temperatures below 500 °C. Finally, the homogeneity of phase compositions across

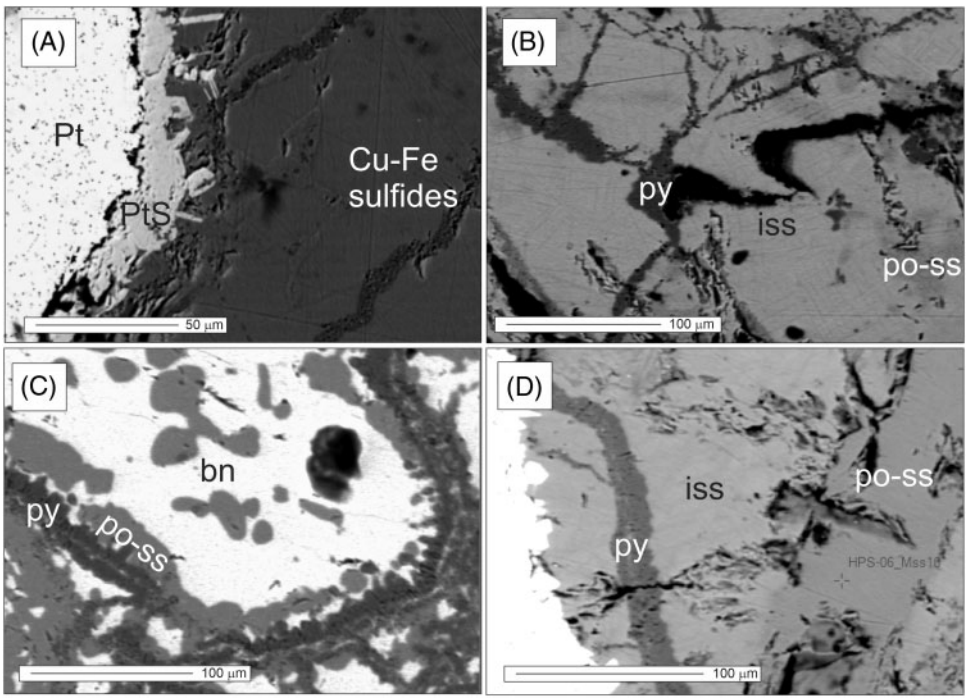

Fig. 4. Backscattered electron images of run products of experiments. (a) HPS 05 (1·0 GPa, 650 °C), showing idiomorphic PtS crystals lining the contact between Cu–Fe–S phases and the Pt capsule wall. (b) HPS 05 (1·0 GPa, 650 °C), showing exsolved unidentified Cu-rich lamellae within *iss*, pyrite along grain boundaries, and irregular patches of homogeneous po-ss within *iss*. (c) HPS 01 (1·7 GPa, 650 °C), showing bornite and po-*ss* replacing original chalcopyrite and pyrite along original grain boundaries. (d) HPS 06 (1·2 GPa, 650 °C) showing pyrite lining former grain boundaries of chalcopyrite (now *iss*) and patches of homogeneous po-*ss*.

Table 5: Thermodynamic properties at 1 bar, 25 °C

Mineral or species	ΔH_f (kJ mol^{-1})		ΔS_f (J mol^{-1})		ΔV_{solid} (J bar^{-1})	
	R	S	R	S	R	S
Pyrite	−171·5	−171·5	52·9	52·9	2·394	2·394
Troilite	−102·6	−100·4	60·3	60·3	1·82	1·82
Pyrrhotite	−97·5	—	60·7	—	1·749	—
Chalcopyrite	−194·9	−186·0	124·9	130·3	4·392	4·283
Covellite	−54·6	−52·3	67·4	66·5	2·042	2·042
Chalcocite	−83·9	−79·5	116·2	120·9	2·748	2·748
Bornite	−371·6	−334·4	398·5	415·4	9·873	9·86
S_2 gas	128·6	128·4	228·17	228·2	2478·97	—

R, Robie & Hemingway (1995) thermodynamic properties; S, Johnson *et al.* (1992).

individual grains, regardless of grain size or identity of texturally associated phases, is highly suggestive that the mineral compositions were equilibrated at run conditions.

THERMODYNAMIC ANALYSIS AND DISCUSSION

The experimental results indicate that chalcopyrite and *iss* break down with increasing pressure. In this section we first provide a synopsis of the key reactions and chemography in the Cu–Fe–S system, followed by the results of thermodynamic calculations, and a description of the anticipated effect of *P* on the key reactions. A synthesis and discussion of the effect of increasing *P* on other important minerals in the Cu–Fe–S system (e.g. nukundamite, villamaninite, covellite, and bornite), which completes the analysis of the Cu-rich portion of the Cu–Fe–S ternary, is provided in Electronic Appendix 2.

We have used existing thermodynamic data to model and assess the sulfide minerals and phase equilibria characteristic of the deeper portion of subduction zones (as in the New Caledonian eclogites) and the upper mantle lithosphere. Two different internally consistent sources of standard thermodynamic data were used to assess natural sulfide phase relations: these were the SUPCRT92 database (Helgeson *et al.*, 1978; Johnson *et al.*, 1992) and tabulated data from Robie & Hemingway (1995). Table 5 compares the thermodynamic properties of Johnson *et al.* (1992) and Robie

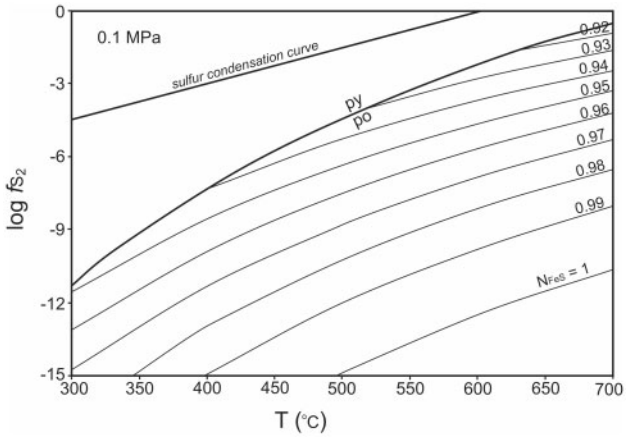

Fig. 5. Composition of pyrrhotite as a function of T and log f_{S_2}. N_{FeS} is the molar fraction of FeS in the system FeS–S_2. Calculated using thermodynamic data from Robie & Hemingway (1995).

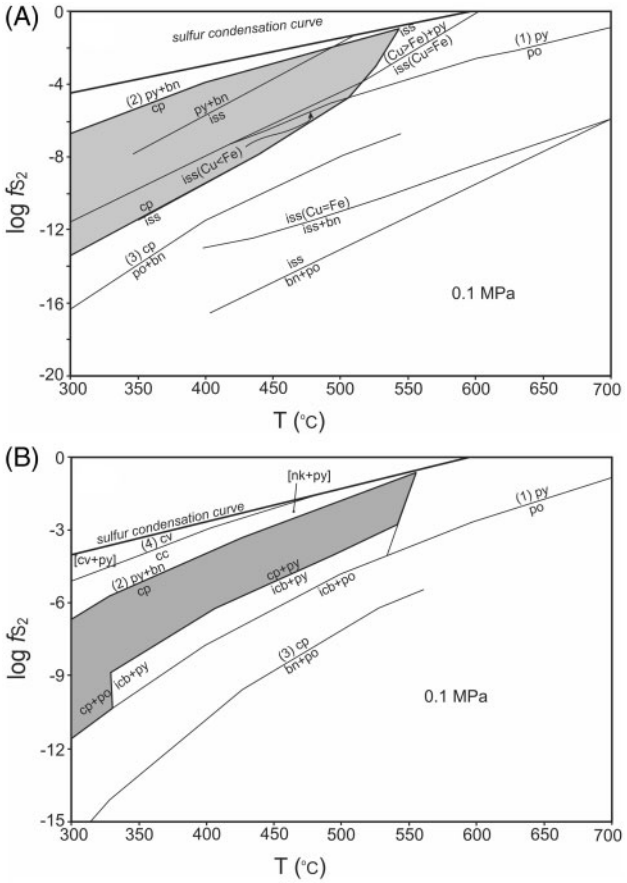

Fig. 6. Reaction boundaries in T, log f_{S_2} space for the Cu–Fe–S system with intermediate solid solution (*iss*) reactions and the sulfur condensation curve. The chalcopyrite stability field is shaded. Experimental data are from (a) Barton (1973) and (b) Lusk & Bray (2002).

& Hemingway (1995) for some of the phases in the three-component Cu–Fe–S system at the standard state of 1 bar and 25 °C.

Standard references consulted for the calculation of phase equilibria include Wood and Fraser (1977), Spear (1993) and Nordstrom & Munoz (1994). Thermodynamic data do not exist for all sulfide minerals in the Cu–Fe–S system, limiting the extent to which their phase relations may be assessed. For example, a complete set of thermodynamic properties for *iss* is unavailable, so Gibbs free energy ($\Delta_r G^o$) for reactions involving this mineral cannot be calculated. *Iss* is a high-temperature, high-entropy mineral $(Cu,Fe)_{1+x}S$ that is broadly isostructural with sphalerite (ZnS) but with Cu and Fe disordered in the cation sites and showing a wide range of relative proportions; the composition range includes those of the lower-temperature ordered minerals cubanite ($CuFe_2S_3$), talnakhite ($Cu_9Fe_8S_{16}$), mooihoekite ($Cu_9Fe_9S_{16}$), putoranite ($Cu_{1.1}Fe_{1.2}S_2$), and haycockite ($Cu_4Fe_5S_8$). Chalcopyrite has a cation-ordered superstructure of the *iss* type, and its composition lies within the *iss* solid solution range. Complete thermodynamic datasets are not available for isocubanite, cubanite or the other *iss* superstructures. Therefore, we adopted chalcopyrite as a proxy for *iss* in calculations relevant to high-pressure sulfide metamorphism. In addition to chalcopyrite, complete thermodynamic properties are available for pyrite, troilite, pyrrhotite, covellite, chalcocite, and stoichiometric bornite, as listed in Table 5. Data from other referenced sources have been used for high digenite and nukundamite where needed.

Calculations and comparison of datasets

Most of the previous work on sulfides in metamorphic environments has focused on ore deposits. Fleet (2006) presented a review of sulfide phase equilibria including the Fe–S, Cu–S, and Cu–Fe–S system, including the work of Kullerud & Yoder (1959), Kullerud (1964), Toulmin & Barton (1964), Yund & Kullerud (1966), Barton (1973), Cabri (1973), Sugaki *et al.* (1975), Kojima & Sugaki (1985), and Lusk & Bray (2002). We relied on these studies (and others as cited) as a basis for our theoretical examination of Cu–Fe sulfide stability at high pressure. A brief summary of the existing literature relevant for this study is presented here.

Chemography and key reactions in the Fe–S, Cu–S, and Cu–Fe–S systems

In the discussion that follows, it should be noted that we refer to sulfur in different ways in different contexts. As a component in the Cu–Fe–S system, it is referred to as S and labelled thus in figures. As a reactant in a mass action expression (i.e. a chemical reaction) it is written as S_2 and is understood to be either a component in a fluid phase or a fugitive component analogous to O_2 in discussions of oxygen fugacity. When we refer to a mass action equation in the text or in figures, we omit S from the equation name, referring instead only to solid phases.

Sulfide relationships in the Fe–S system are very well understood, and are depicted in Fig. 5 (after Toulmin & Barton, 1964). Where pyrite and pyrrhotite

Table 6: *Comparison of log* f_{S_2} *with changing* P *for equilibria, at* T = *427°C (700 K)*

Number	Reaction name	1 bar		0·1 GPa		0·5 GPa		1·0 GPa		2·0 GPa	
		R	S	R	S	R	S	R	S	R	S
1	py = po	−6·43	−6·84	−6·34	−6·76	−6·00	−6·42	−5·57	−5·99	−4·71	−5·13
2	cp = py + bn	−3·26	−3·24	−3·45	−3·38	−4·19	−3·97	−5·13	−4·71	−7·00	−6·19
3	cp = po + bn	−9·59	−10·54	−9·23	−10·13	−7·80	−8·86	−6·01	−7·26	−2·42	−4·08
4	cv = cc	−2·75	−1·91	−2·55	−1·76	−1·76	−0·92	−0·76	0·78	1·23	2·07
5	cp = po + py + bn	n.a.	n.a.	n.a.	n.a.	n.a.	n.a.	n.a.	n.a.	n.a.	n.a.

R, data calculated using Robie & Hemingway (1995) thermodynamic properties; S, data calculated using SUPCRT92, Johnson *et al.* (1992), and Helgeson *et al.* (1978). n.a., not applicable.

coexist, the composition of pyrrhotite is a predictable function of f_{S_2} and T. The Fe–S system will be described before considering the more complex Cu-bearing system. The systematics were described in detail by Brown (2007), based mainly on the work of Toulmin & Barton (1964). The reaction of pyrite to pyrrhotite,

$$\underset{\text{pyrite}}{FeS_2} = (^{1}/_{1-x})\underset{\text{pyrrhotite}}{Fe_{1-x}S} + (^{1-2x}/_{2-2x})S_2$$

which can be simplified for $x = 0$ to

$$FeS_2 = FeS + 0{\cdot}5S_2 \qquad (1)$$

appears as a curve in log f_{S_2} vs T space, shown at 1 bar in Figs 5 and 6. The pyrite–pyrrhotite reaction can be described as a geothermometer: the Fe content in pyrrhotite changes with T and f_{S_2}. Pyrrhotite coexists with pyrite along the py = po [reaction (1)] curve indicated in the figures. In the equations below, thermodynamic data for troilite (FeS), which is the iron-rich end-member of the high-temperature hexagonal pyrrhotite polytype, are used as proxies for those of end-member pyrrhotite with $x = 0$. The S condensation curve has been measured experimentally both by Barton (1973) and by Lusk & Bray (2002). At f_{S_2} below the S condensation curve, S_2 is a component in a hypothetical gas phase that need not be physically present for sulfur fugacity to be a useful thermodynamic parameter. Above the S condensation curve, and in any chemographic triangle in the figures and discussion below where one vertex of a triangle is S, f_{S_2} may or may not be high enough to stabilize a condensed sulfur phase, either liquid or solid. Our experimental run products do not contain a condensed sulfur phase, because all of them contain the stable assemblage py + po *ss*, which is far below the S condensation curve in Fig. 5.

Published low-*P* phase relations for the Cu–Fe–S system from Barton (1973) and Lusk & Bray (2002) can be used to define a chalcopyrite stability field (in grey, Fig. 6) limited by the reaction of chalcopyrite to bornite and pyrite at high f_{S_2} and by the reaction of chalcopyrite to *iss* (with Cu:Fe = 1:1, isochemical with chalcopyrite; Fig. 6a) or isocubanite (*iss* with Cu:Fe = 1:2 and hence not isochemical; Fig. 6b) at low f_{S_2}. Also shown are reactions (1)–(3) of Table 3, as calculated with Johnson *et al.* (1992) data. The upper f_{S_2} limit of chalcopyrite stability, cp = py + bn,

$$\underset{\text{chalcopyrite}}{5CuFeS_2} + S_2 = \underset{\text{pyrite}}{4FeS_2} + \underset{\text{bornite}}{Cu_5FeS_4}, \quad \Delta V_{\text{solid}} = -2{\cdot}511\ \text{J bar}^{-1} \qquad (2)$$

can be modelled easily with thermochemical data. In contrast to this, the lower f_{S_2} limit of the chalcopyrite stability field is determined by its breakdown to *iss*, a phase of variable composition for which thermodynamic data are not available. Figure 6a and b shows that a change in *iss* composition can move the boundary in T–f_{S_2} space. Thus, we represent the low f_{S_2} limit of *iss* stability by the reaction cp = po + bn:

$$\underset{\text{chalcopyrite}}{5CuFeS_2} = \underset{\text{pyrrhotite}}{4FeS} + \underset{\text{bornite}}{Cu_5FeS_4} + S_2, \quad \Delta V_{\text{solid}} = -4{\cdot}807\ \text{J bar}^{-1} \qquad (3)$$

even though in reality this reaction is known to be metastable owing to the replacement of ordered chalcopyrite by *iss* and Fe sulfides (Fig. 6b). Chalcopyrite in this model will thus appear to occupy a slightly larger stability field in f_{S_2} vs T space than it does in reality, extending to lower f_{S_2}.

Table 6 compares log f_{S_2} values for equilibria at 427 °C (700 K) at various pressures estimated using the databases of both Johnson *et al.* (1992) and Robie & Hemingway (1995). This temperature has been experienced by most of the New Caledonian high-pressure belt. Table 7 shows the corresponding differences in the Gibbs free energy of the reactions, $\Delta_r G^\circ$. Because log f_{S_2} values are different between datasets (Table 5), the values for Gibbs free energy of reaction also show differences (Table 7 and Fig. 7). There is almost no difference between datasets in calculated $\Delta_r G^\circ$ for the reaction between pyrite and pyrrhotite, whereas reactions of chalcopyrite to pyrite + bornite, to pyrite + pyrrhotite + bornite and to pyrrhotite + bornite show some divergence with increasing pressure; the reaction between covellite and chalcocite is consistently different. The variability between datasets illustrated in Fig. 7 results in consistent differences in position of calculated phase boundaries portrayed on phase diagrams, but the topologies remain the same.

Table 7: *Comparison of* ΔG *(in J mol^{-1}) with changing* P *for equilibria, at* T = *427°C (700 K)*

Number	Reaction name	1 bar		0·1 GPa		0·5 GPa		1·0 GPa		2·0 GPa	
		R	S	R	S	R	S	R	S	R	S
1	py = po	43060	45873	42487	45300	40191	43007	37321	40137	31581	34367
2	cp = py + bn	−43674	−43371	−46183	−45350	−56227	−53266	−68782	−63161	−93892	−82952
3	cp = po + bn	128566	140126	123764	135859	104536	118754	80501	97383	32431	54630
4	cv = cc	18443	12841	17108	11506	11764	6159	5084	−519	−8275	−13878
5	cp = po + py + bn	42446	48375	38791	45254	24155	32744	5860	17108	−30730	−14163

For reaction (5) (solid–solid) at 700 K, for R, P = 1·16 GPa; for S, P = 1·55 GPa. R, data calculated using Robie & Hemingway (1995) thermodynamic properties; S, data calculated using SUPCRT92, Johnson *et al.* (1992), and Helgeson *et al.* (1978).

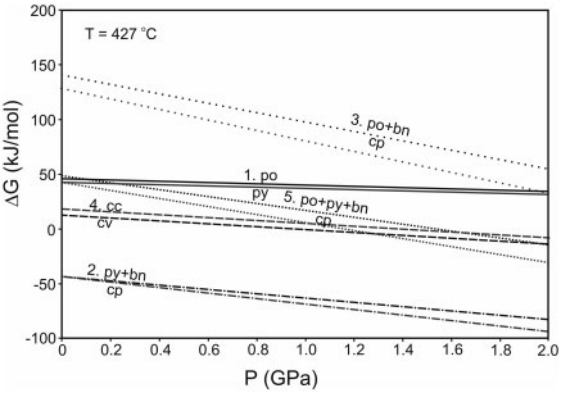

Fig. 7. ΔG vs P for reactions (1)–(5) (Table 3). Lines calculated using data of Johnson *et al.* (1992) are black; those calculated with data of Robie & Hemingway (1995) are grey. There is almost no difference in ΔG for py–po (1), whereas ΔG diverges for cp−py + bn (2), cp−po + bn (3), and cp−po + py + bn (5) and is consistently different for cv–cc (4).

Description of the effect of pressure on phase equilibria

The effect of pressure on Fe–S phase equilibria

High-pressure phase relations in the Fe–S system have been explored to high T and P, and the pyrite–pyrrhotite relation persists to P and T conditions well beyond those found along the Earth's subduction geotherms. Toulmin & Barton (1964, fig. 13) calculated the effect of pressure on the S condensation curve up to 0·5 GPa. Their result is used here in Figs 5, 6 and 8, and extrapolated to 2·0 GPa in Fig. 8. The initial values for the curve have been taken from Lusk & Bray (2002). The S condensation curve shifts toward higher f_{S_2} with increasing P. All of the reactions considered in this study occur at sulfur fugacities so far below sulfur condensation that our treatment of the reactions as solid–solid equilibria is justified.

A description and discussion of the pressure effects on the Cu-rich portion of the Cu–Fe–S ternary, including an analysis of nukundamite and villamaninite, is presented in Electronic Appendix 2.

Pyrite–pyrrhotite

The location of the pyrite–pyrrhotite reaction shifts by ∼2·5 log units of f_{S_2} over the range 0–2·0 GPa, with only a small difference between datasets (Table 6). Isopleths of Fe content in pyrrhotite are plotted for reference in Fig. 5. It should be noted that the pyrrhotite composition parameter N_{FeS} is the mole fraction of FeS in the system FeS–S_2, and differs from Fe content in pyrrhotite as denoted by the '1–x' term in $Fe_{1-x}S$, where $x = (1 - N)/(1 + N)$. The pressure effect is calculated as was done by Toulmin & Barton (1964) and refined by Scott (1973). The activity of FeS in pyrrhotite with changing pressure was calculated following Craig & Scott (1974, page CS-39) using the volume data given by Toulmin & Barton (1964) and Scott (1973). Pyrrhotite isopleths shift toward higher f_{S_2} with increasing pressure (Fig. 8). Therefore, one might assume that pyrrhotite with lower Fe contents (e.g. with N_{FeS} = 0·92) would shift beyond the pyrite–pyrrhotite curve, and thus no longer be stable. However, the pyrite–pyrrhotite reaction also shifts toward higher f_{S_2} conditions with increasing P, as does the sulfur condensation curve, so metal-deficient pyrrhotite remains stable at higher P.

Cu–Fe–S phase equilibria

It is assumed that with changing P, T, and f_{S_2}, the stability field for chalcopyrite will approximate to that of disordered *iss* of near-chalcopyrite composition. The use of chalcopyrite reactions is warranted because chalcopyrite is stable up to ∼550 °C, and $CuFeS_2$ is a composition that lies within the *iss* range above that temperature. Molar volume data are available only for isocubanite, a cubic polymorph of cubanite specified by Caye *et al.* (1988) to be the mineral previously described as 'chalcopyrrhotite', 'cubanite II', 'cubic cubanite', and 'intermediate solid solution'. In fact, isocubanite is equivalent to natural *iss* with Cu:Fe = 1:2. Using the molar volume of isocubanite as a proxy for that of *iss*, the direction of reaction progress during pressure increase of reactions involving *iss* with isocubanite composition may be determined. Although thermodynamic evaluation is limited because of the lack of data for the *iss*, f_{S_2}–T and P–T plots for chalcopyrite-bearing assemblages will give at least an indication of the nature of the Cu–Fe–S system phase topological evolution at high pressure, given the close structural and compositional similarity between chalcopyrite and *iss*.

Lusk & Bray (2002) defined a covellite stability field [shown as (cv + py) in Fig. 6b], which is very similar to reaction (4) in Table 3 (cv = cc):

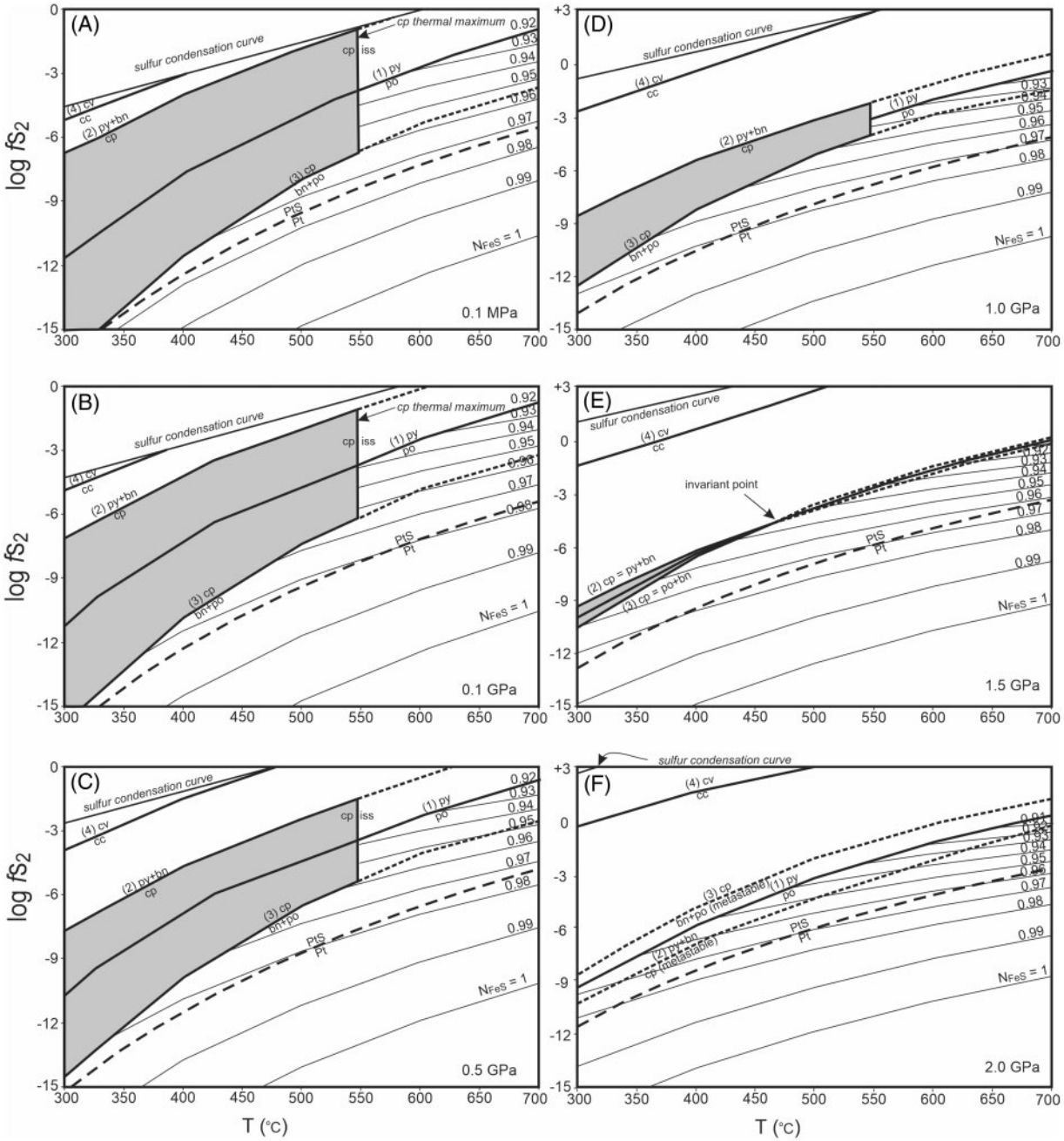

Fig. 8. log f_{S_2} vs T for some reactions in the Cu–Fe–S system at 1 bar, 0·1 GPa, 0·5 GPa, 1·0 GPa, 1·5 GPa, and 2·0 GPa. The shaded area corresponds to chalcopyrite stability. Dashed lines are metastable reactions. Calculated using data from Johnson *et al.* (1992). Long-dashed lines show f_{S_2} at the Pt–PtS buffer.

$$\underset{\text{covellite}}{2CuS} = \underset{\text{chalcocite}}{Cu_2S} + 0{\cdot}5S_2, \quad \Delta V_{\text{solid}} = -1{\cdot}336\,\text{J bar}^{-1} \tag{4}$$

using Johnson *et al.* (1992) data. The corresponding stable equilibrium line for covellite breakdown to the actual breakdown product in the absence of Fe, high digenite, is very close but less curved, intersecting the sulfur saturation line at 507 °C and lying about 0·5 log unit higher in f_{S_2} at 300 °C (Seal *et al.*, 2001). We calculate and plot in Fig. 6b the conditions for this reaction along the Fe-free Cu–S join using chalcocite instead of using bornite-*ss* or its Fe-free end-member high digenite because we lack data for either composition and assume that chalcocite has similar properties to high digenite, its high-temperature disordered polytype.

Stability of chalcopyrite at high pressure

Using either thermodynamic dataset, the stability field of chalcopyrite narrows with increasing pressure. Figure 8 illustrates the pressure dependence of chalcopyrite stability using Johnson *et al.* (1992) data; the same topology with some differences can be illustrated using data of

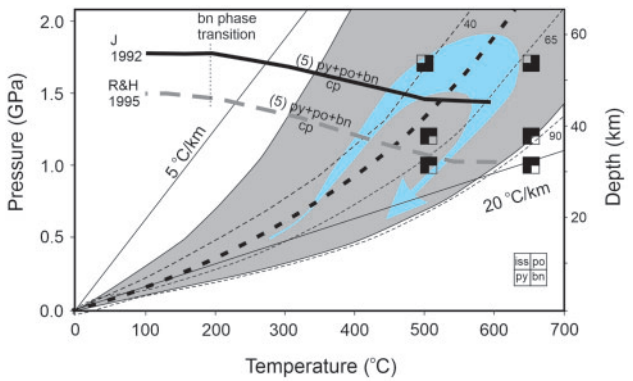

Fig. 9. Comparison of chalcopyrite (or, semi-quantitatively, *iss*) stability from experiments and the two thermodynamic datasets. Curves labeled R&H 1995 and J 1992 show reaction (5), cp = py + po + bn, calculated using the databases of Robie & Hemingway (1995) and SUPCRT92 of Johnson *et al.* (1992), respectively. The difference in chalcopyrite stability limit between datasets is 0·25 GPa at low T to 0·45 GPa at higher T. Experimental phase assemblages (inset box at lower right) indicate that calculations based on the Johnson *et al.* (1992) database are the more accurate. Also shown in grey is the field of measured P–T conditions for a global compilation of subduction terranes (Penniston-Dorland *et al.*, 2015). The blue arrow shows the P–T path followed by the New Caledonian high-pressure belt (Clarke *et al.*, 1997; Carson *et al.*, 1999; Marmo *et al.*, 2002; Fitzherbert *et al.*, 2003). The bold dashed black line is the steady-state oceanic geotherm (McKenzie *et al.*, 2005). Light black dashed lines are the continental geotherm for surface heat flows of 40, 65, and 90 mW/m^2 (Jaupart & Mareschal, 2007). This diagram shows that chalcopyrite in New Caledonian eclogite and in samples of upper mantle lithospheric peridotite is retrograde, not after *iss* as is commonly assumed, but after an assemblage dominated by bornite–digenite solid solution.

Robie & Hemingway (1995; not shown here). At 0·1 GPa the gap between covellite and chalcopyrite stability begins to enlarge, otherwise the calculated equilibria remain fairly similar. At 0·5 GPa, the chalcopyrite field is noticeably smaller than at 0·1 GPa (Fig. 8). At 1·0 GPa, only a narrow chalcopyrite field remains. By 1·5 GPa, the field of chalcopyrite stability is predicted to be completely absent by the Robie & Hemingway dataset (not shown) whereas the field of chalcopyrite stability is much reduced but still present when the Johnson *et al.* (1992) dataset is used (Fig. 8). In both datasets, chalcopyrite no longer has any stability field in f_{S_2}–T space at 2·0 GPa. Instead, the association of py + po + bn is characteristic of high pressures.

Thus, using either dataset, the range of f_{S_2} and T at which chalcopyrite is stable decreases with increasing pressure. In Fig. 8, the final disappearance of chalcopyrite occurs at an invariant point that corresponds to the intersection of the cp = py + bn [reaction (2)] and cp = po + bn [reaction (3)] curves with the py = po [reaction (1)] curve. This point also corresponds to the volatile-free terminal breakdown reaction (5), where chalcopyrite is replaced by pyrite + pyrrhotite + bornite:

$$\underset{\text{chalcopyrite}}{5CuFeS_2} = \underset{\text{pyrrhotite}}{2FeS} + \underset{\text{pyrite}}{2FeS_2} + \underset{\text{bornite}}{Cu_5FeS_4}, \quad \Delta V_{\text{solid}} = -3{\cdot}659\ \text{J bar}^{-1}. \tag{5}$$

As reaction (5) is independent of f_{S_2}, it can be plotted directly on a P–T diagram with no need to specify f_{S_2}, unlike univariant reactions involving S_2 whose curves will appear in different places depending on f_{S_2} (Fig. 9). Table 7 gives equilibrium pressures at 427 °C of 1·16 GPa and 1·55 GPa for Robie & Hemingway (1995) and Johnson *et al.* (1992) respectively. This ~0·4 GPa difference is slightly narrower toward 200 °C, and broadens to ~0·5 GPa at 550 °C. In Fig. 8, the P–T path for eclogite-facies metamorphism [based on Clarke *et al.* (1997), Carson *et al.* (1999), Marmo *et al.* (2002), and Fitzherbert *et al.* (2003)] is overlain with reaction (5), from both datasets. The implication is that all chalcopyrite now present in eclogites, subducted to P of 1·1–1·5 GPa, must be retrograde.

Figure 2 shows the relative locations in the Cu–Fe–S ternary system of the phases py, po, cp and bn that participate in reactions at the invariant point. It should be stressed that at high temperatures, the compositional range of bn-*ss* extends to the Fe-free end-member dg, so there is a single bn–dg–cc solid solution that we refer to simply as bn-*ss* or bornite–digenite *ss*. The topology of reactions (1), (2), (3) and (5) in P–T space and the stability field of cp are depicted qualitatively in Fig. 10a, and P-T conditions for the reactions are shown more quantitatively as a function of f_{S_2} in Fig. 10b. It should be noted how the high-P stability limit for cp (and, given their similarity, *iss*) decreases with increasing T and f_{S_2}, as defined by reactions cp = py + po + bn [reaction (5)] and cp = po + bn [reaction (3)].

Figure 8 shows log f_{S_2}–T plots of reactions (1)–(4) in Table 3 calculated using Johnson *et al.* (1992). The topology of the system in log f_{S_2}–T space is very similar for both the Robie & Hemingway (1995) and Johnson *et al.* (1992) datasets (Brown, 2007), although some pressure–dependent differences exist (not shown). In particular, reactions (2) cp = py + bn and (3) cp = po + bn, defining the upper and lower f_{S_2} limits of chalcopyrite respectively, differ in locations, owing to large differences between the datasets in H and S data for bornite at 25 °C. There are also less marked discrepancies between the two datasets for chalcopyrite, chalcocite, and covellite.

Whereas the cp = bn + py equilibrium curve (2) is almost identical in both datasets, there is an almost constant offset of 0·42 log f_{S_2} units difference between datasets for the py = po curve (1), as shown in Tables 6 and 7. This consistent shift can be attributed to the different enthalpies of formation for troilite (Table 5), the only parameters relevant to reaction (1) that differ between the two datasets. For other reactions, differences in thermodynamic state variables for the various phases (Table 5) lead to curves calculated for the two datasets that diverge with increasing pressure (Table 6). There is also a significant difference of almost 1 log unit for f_{S_2} along both the cv = cc curve (4) and the cp = po + bn curve (3) even at P conditions of 1 bar.

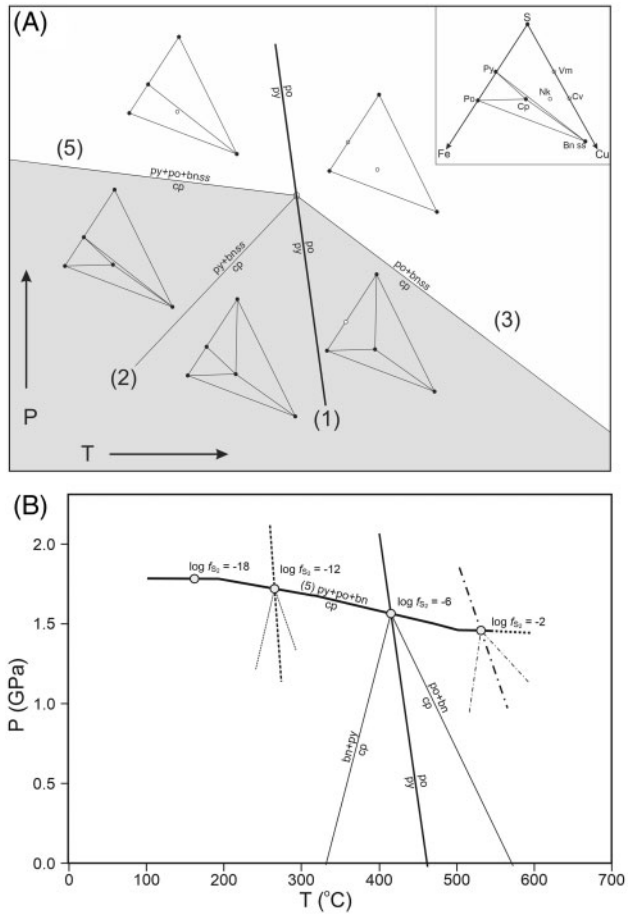

Fig. 10. (a) Schreinemaker's construction for a portion of the Cu–Fe–S composition triangle. Reaction numbers are those of Table 3. Top right inset shows relative placement and tie-line topology for specific compositions of pyrite (Py), pyrrhotite (Po), chalcopyrite (Cp) and bornite solid solution (Bn ss) stable together at low-*T*, moderate-*P* conditions (e.g. 300 °C, 1·0 GPa). Open circles show Cu-rich phases that are probably unstable under these conditions and not considered here but are discussed in Electronic Appendix 2: nukundamite (Nk), covellite (Cv), and villamaninite (Vm). The Schreinemaker's construction is for univariant phase equilibria involving Py, Po, Cp, Bn and S, surrounding an invariant point. Reaction (5) is stable only to the left of this point, and is replaced by reaction (3) at higher *T*. The stability field for Cp is shaded, and unstable phases are indicated by open circles. Degenerate pyrite breakdown reaction (1) is shown in bold. It should be noted that volatile-absent reaction (5) is stable only to the low-*T* side of the invariant point. (b) Quantitative *P*–*T* diagram shows the position of volatile-absent Cp breakdown reaction (5) according to Johnson *et al.* (1992), with calculated positions of the Py + Po + Cp + Bn + S invariant point as a function of f_{S_2}. Placement of volatile-bearing reactions from (a) are shown at log $f_{S_2} = -6$, and also their displacement for log $f_{S_2} = -12$ and -2.

Comparison of experimental data with predictions from thermochemistry

Our experiments were not conducted with deliberate internal buffering of fugacity for sulfur or oxygen. All run products contain apparently stably coexisting pyrite and pyrrhotite, which define an f_{S_2} buffer as shown in Fig. 8. The exact position of the py–po f_{S_2} buffer in Fig. 8 will be affected by the presence of measurable quantities of Cu in both phases, which would make the reaction divariant if Cu activity was not controlled. However, if the activity of CuS is buffered in both phases by their simultaneous coexistence with either *iss* or *bnss* then the reaction will still be effectively univariant although the precise value of f_{S_2} at which it occurs at a given *T* may not be as predicted for the degenerate reaction py–po. The sulfur fugacity of the observed ubiquitous assemblage pyrite–pyrrhotite can be compared with the Pt–PtS solid buffer. The experiments at 650 °C and 1·0 or 1·2 GPa contain both Pt and PtS whereas the other experiments contained only Pt. Using data from Johnson *et al.* (1992), we estimate log f_{S_2} at the Pt–PtS buffer (Fig. 8). All the observed run product assemblages contain pyrite and pyrrhotite and therefore equilibrated at f_{S_2} above the Pt–PtS buffer. At 650 °C the kinetics were evidently sufficiently rapid to force the capsule material to react with S_2 in the experimental charge and produce a visible coating of PtS separating unreacted Pt from the sulfide phases. At run temperatures below 650 °C, although the f_{S_2} of the system was internally buffered by the pyrite–pyrrhotite reaction, the Pt capsule failed to react in a way that would generate an observable coating of PtS. It is conceivable but seems unlikely that the effect of Cu on the py–po equilibrium depressed f_{S_2} to values below the Pt–PtS buffer in the lower temperature experiments, accounting therefore for the absence of PtS in these run products.

Regardless of the precise value of f_{S_2} in our experiments, our observations confirm the experimental determination by Barton (1973) that chalcopyrite is replaced by relatively metal-rich *iss* at low f_{S_2} as shown in Fig. 6a. Additionally, the replacement of *iss* by bornite in the two runs at 1·7 GPa confirms our arguments above on thermodynamic grounds that there is no field of stability for chalcopyrite or *iss* at pressures exceeding some limit that lies between 1·5 and 1·7 GPa.

Comparison with the experimental phase assemblages shows that the Johnson *et al.* (1992) database successfully models the experimental results (e.g. Fig. 9) and hence should predict natural high-pressure phase equilibria with reasonable accuracy. Any subducted terrane should have undergone chalcopyrite/*iss* breakdown, if it has experienced *P*–*T* conditions similar to those of the New Caledonian eclogites. This observation also applies to portions of upper mantle lithosphere.

A major finding of this experimental study is that chalcopyrite is no longer stable above ~1·5 GPa (this study), 550 °C (Barton, 1973) and breaks down to an assemblage of bornite/digenite, pyrite, and pyrrhotite [reaction (5)]. This is consistent with the inclusion assemblages observed from New Caledonian blueschist and eclogite documented by Brown *et al.* (2014). At higher *T* and lower f_{S_2}, where pyrite is unstable, the corresponding products are bornite–digenite solid solution, pyrrhotite + fluid-phase S_2 [reaction (3), Fig. 8].

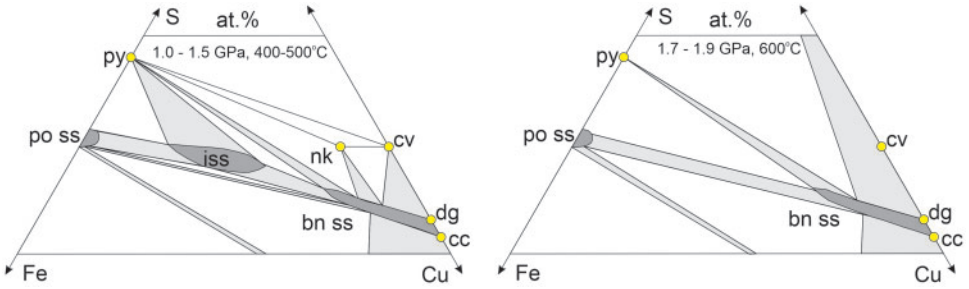

Fig. 11. Chemography of the Fe–Cu–S system at high pressure as calculated using data from Johnson *et al.* (1992) and partially confirmed by experiment in this study. Details of the reactions involving nukundamite and covellite are described in Electronic Appendix 2.

The deep sulfur cycle

Two observations about the evolution of Cu–Fe sulfide assemblages during prograde metamorphism have implications for the deep sulfur cycle. Copper enrichment in sulfide with high-pressure metamorphism (Brown *et al.*, 2014) indicates that Fe is incorporated into garnet as a lithophile element, tending to raise f_{S_2}, leaving Cu to be correspondingly concentrated in sulfide minerals and promoting loss of S in fugitive volatile phases. Thus, Cu/Fe ratio in the sulfide inclusion suites increases with pressure. This is consistent with the results of this study; experiments and phase equilibria calculations both indicate that the Cu sulfide stable at the high *P* consistent with conditions in deeper parts of subduction zones and in the lithospheric mantle is bornite–digenite solid solution, with a higher metal/sulfur ratio [(Cu + Fe)/S] than chalcopyrite/*iss* (Figs 3 and 11). The relatively S-poor sulfide compositions observed in high-pressure assemblages need not result from equilibration at low f_{S_2}, and a corresponding depletion of sulfur from whole-rocks during subduction is therefore not surprising (see Evans *et al.*, 2014). However, a system with a given Cu content might be capable of accommodating a higher S content at still higher *P* if villamaninite (described in Electronic Appendix 2) becomes stable, with its low (Cu + Fe)/S ratio.

The behaviour of trace chalcophile elements in the lithospheric mantle is thought to be sensitive to the presence or absence of sulfide liquid. At temperatures between the solidus of pyrrhotite solid solution in mantle sulfide and the liquidus of the associated Cu-rich sulfide liquid, it would follow that the chalcophile elements can be fractionated from each other by physical separation of po-*ss* and sulfide liquid. The final Cu-rich sulfide solid that forms during cooling of the Cu-rich sulfide liquid is generally assumed to be *iss* (e.g. Lorand & Alard, 2001; Lorand et al., 2013). Our results show that along a cool subcontinental geotherm, the principal Cu sulfide mineral is likely to be bornite–digenite solid solution over the pressure range 1·5–2·0 GPa, corresponding to a depth of about 45–65 km and, for the cool geothermal gradients corresponding to the *P–T* trajectory of the New Caledonian rocks, temperatures of 450–650 °C (Fig. 8). At still greater depths, pressures, and temperatures, the more S-rich but also very Cu-rich villamaninite may prevail. Although little is known as yet about the partitioning of chalcophile elements among bornite–digenite *ss*, po-*ss*, *iss*, and sulfidic fluid or melt, we suggest that use of data such as trace element partition coefficients obtained for *iss*–sulfide melt equilibrium in modeling of low-temperature volatile-fluxed melting may lead to significant errors in estimating chalcophile element behavior in both the oceanic and subcontinental lithosphere.

CONCLUSIONS

Experiments and phase equilibria calculations using two thermodynamic datasets show that the range of possible stable phases in the Cu–Fe–S system becomes smaller with increasing temperature and pressure. Chalcopyrite is replaced by *iss* at moderate temperature and 1 GPa, and it undergoes a terminal breakdown reaction between 1·0 and 1·7 GPa. Nukundumite and covellite undergo similar terminal breakdowns. At the highest temperature and pressure conditions addressed in our study, it appears that the only assemblage likely to occur in systems well below the sulfur condensation curve and not saturated with a metallic phase is pyrite + pyrrhotite + bornite-*ss*. Comparison of the experimental results with available thermochemical data also showed that calculations using the database of Johnson *et al.* (1992) predicted the stability limit of chalcopyrite, for the conditions investigated, more accurately than did calculations using the Robie & Hemingway (1995) data.

The only sub-solidus Cu sulfide mineral characteristic of the deeper portions of subduction zones and of the shallow lithospheric mantle at depths greater than the 1·7 GPa isobar and temperatures below the melting temperature of bornite is therefore bornite solid-solution, not intermediate solid solution as is commonly supposed.

ACKNOWLEDGEMENTS

Reviews from T. Kawakami, K. Evans and an anonymous reviewer, and editorial oversight from J. Hermann were very useful for clarifying our findings.

FUNDING

J.L.B. acknowledges support from the Australian National University. J.E.M. acknowledges the support of a Canadian Natural Sciences and Engineering Research Council Discovery Grant.

SUPPLEMENTARY DATA

Supplementary data are available at *Journal of Petrology* online.

REFERENCES

Barin, I. (1995). *Thermochemical Data of Pure Substances*. New York: Weinheim, 1885 pp.

Barton, P. B. (1973). Solid-solutions in system Cu–Fe–S Part 1. Cu–S and Cu–Fe–S Joins. *Economic Geology* **68**, 455–465.

Bayliss, P. (1989). Crystal chemistry and crystallography of some minerals within the pyrite group. *American Mineralogist* **74**, 1168–1176.

Brown, J. L. (2007). The deep sulfur cycle: Insights from prograde sulfide metamorphism in blueschist and eclogite, northeastern New Caledonia. PhD thesis, Australian National University, Canberra, ACT.

Brown, J. L., Christy, A. G., Ellis, D. J. & Arculus, R. J. (2014). Prograde sulfide metamorphism in blueschist and eclogite, New Caledonia. *Journal of Petrology* **55**, 643–670.

Cabri, L. J. (1973). New data on phase relations in Cu–Fe–S system. *Economic Geology* **68**, 443–454.

Cabri, L. J. & Hall, S. R. (1972). Mooihoekite and haycockite two new copper–iron sulfides and their relationship to chalcopyrite and talnakhite. *American Mineralogist* **57**, 689–708.

Carson, C. J., Powell, R. & Clarke, G. L. (1999). Calculated mineral equilibria for eclogites in $CaO–Na_2O–FeO–MgO–Al_2O_3–SiO_2–H_2O$: application to the Pouebo Terrane, Pam Peninsula, New Caledonia. *Journal of Metamorphic Geology* **17**, 9–24.

Carson, C. J., Clarke, G. L. & Powell, R. (2000). Hydration of eclogite, Pam Peninsula, New Caledonia. *Journal of Metamorphic Geology* **18**, 79–90.

Caye, R., Cervelle, B., Cesbron, F., Oudin, E., Picot, P. & Pillard, F. (1988). Isocubanite, a new definition of the cubic polymorph of cubanite $CuFe_2S_3$. *Mineralogical Magazine* **52**, 509–514.

Chen, J. H. & Harvey, W. W. (1974). Cation self-diffusion in chalcopyrite and pyrite. *Metallurgical Transactions B* **6B**, 331–337.

Clarke, G. L., Aitchison, J. C. & Cluzel, D. (1997). Eclogites and blueschists of the Pam Peninsula, NE New Caledonia: a reappraisal. *Journal of Petrology* **38**, 843–876.

Condit, R. H., Hobbins, C. E. & Birchenall, C. E. (1974). Self-diffusion of iron and sulfur in ferrous sulfide. *Oxidation of Metals* **8**, 408–455.

Craig, J. R. & Scott, S.D. (1974). Sulfide phase equilibria. In: Ribbe, P. H. (ed.) *Mineralogical Society of America, Reviews in Mineralogy* **1**, CS-1 - CS-110.

Evans, K. A., Tomkins, A., Cliff, J. & Fiorentini, M. L. (2014). Insights into subduction zone sulfur recycling from isotopic analysis of eclogite-hosted sulfides. *Chemical Geology* **365**, 1–19.

Fitzherbert, J. A., Clarke, G. L. & Powell, R. (2003). Lawsonite–omphacite-bearing metabasites of the Pam Peninsula, NE New Caledonia: evidence for disrupted blueschist- to eclogite-facies conditions. *Journal of Petrology* **44**, 1805–1831.

Fleet, M. E. (2006). Phase Equilibria at High Temperatures. *Reviews in Mineralogy and Geochemistry* **61**, 365–419.

Grguric, B. A., Harrison, R. J. & Putnis, A. (2000). A revised phase diagram for the bornite–digenite join from *in situ* neutron diffraction and DSC experiments. *Mineralogical Magazine* **64**, 213–231.

Helgeson, H. C., Delany, J. M., Nesbitt, H. W. & Bird, D. K. (1978). Summary and critique of the thermodynamic properties of rock-forming minerals. *American Journal of Science* **278A**.

Inan, E. E. & Einaudi, M. T. (2002). Nukundamite ($Cu_{3.38}Fe_{0.62}S_4$)-bearing copper ore in the Bingham porphyry deposit, Utah: Result of upflow through quartzite. *Economic Geology* **97**, 499–515.

Jaupart, C. & Mareschal, J.-C. (2007). Heat flow and thermal structure of the lithosphere. In: Watts, A. B. (ed.) The lithosphere. *Treatise on Geochemistry*, **6**. Amsterdam: Elsevier, pp. 218–251.

Jenner, F. E., Arculus, R. J., Mavrogenes, J. A., Dyriw, N. J., Nebel, O. & Hauri, E. H. (2012). Chalcophile element systematics in the volcanic glasses from the northwestern Lau Basin. *Geochemistry, Geophysics, Geosystems* **13**, Q06014.

Johnson, J. W., Oelkers, E. H. & Helgeson, H. C. (1992). SUPCRT92: a software package for calculating the standard molal thermodynamic properties of minerals, gases, aqueous species and reactions from 1 to 5000 bar and 0 °C to 1000 °C. *Computers & Geosciences* **18**, 899–947.

Kajiwara, Y. (1969). Fukuchilite, Cu_3FeS_8, a new mineral from the Hanawa mine, Akita Prefecture, Japan. *Mineralogical Journal* **5**, 399–416.

Kojima, S. & Sugaki, A. (1985). Phase relations in the Cu–Fe–Zn–S system between 500° and 300 °C under hydrothermal conditions. *Economic Geology* **80**, 158–171.

Kullerud, G. (1964). The Cu–Fe–S system. *Carnegie Institution of Washington, Yearbook* **63**, 200–202.

Kullerud, G. & Yoder, H. S. (1959). Pyrite stability relations in the Fe-S system. Economic Geology **54**, 533–572.10.2113/gsecongeo.54.4.533

Lorand, J.-P., Luguet, A. & Alard, O. (2013). Platinum-group element systematics and petrogenetic processing of the continental upper mantle: A review. Lithos **164-167**, 2–21.

Lorand, J.-P. & Alard, O. (2001). Platinum-group element abundances in the upper mantle: new constraints from in situ and whole-rock analyses of Massif Central xenoliths (France). Geochimica Et Cosmochimica Acta **65**, 2789–2806.

Lusk, J. & Bray, D. M. (2002). Phase relations and the electrochemical determination of sulfur fugacity for selected reactions in the Cu–Fe–S and Fe–S systems at 1 bar and temperatures between 185 and 460 °C. *Chemical Geology* **192**, 227–248.

Marcos, C., Paniagua, A., Moreiras, D. B., Garcia-Granda, S. & Diaz, M. R. (1996). Villamaninite, a case of noncubic pyrite-type structure. *Acta Crystallographica Section B—Structural Science* **52**, 899–904.

Marmo, B. A., Clarke, G. L. & Powell, R. (2002). Fractionation of bulk rock composition due to porphyroblast growth: effects on eclogite facies mineral equilibria, Pam Peninsula, New Caledonia. *Journal of Metamorphic Geology* **20**, 151–165.

McKenzie, D., Jackson, J. & Priestly, K. (2005). Thermal structure of oceanic and continental lithosphere. *Earth and Planetary Science Letters* **233**, 337–349.

Merwin, H. E. & Lombard, R. H. (1937). The system Cu–Fe–S. *Economic Geology* **32**, 203–284.

Morimoto, N. & Kullerud, G. (1963). Polymorphism in digenite. *American Mineralogist* **48**, 110–123.

Morimoto, N. & Kullerud, G. (1966). Polymorphism on the Cu_9S_5–Cu_5FeS_4 join. *Zeitschrift fur Kristallographie* **123**, 235–254.

Mungall, J., Andrews, R. A., Cabri, L. J., Sylvester, P. J. & Tubrett, M. (2005). Partitioning of Cu, Ni, Au, and platinum-group elements between monosulfide solid solution and sulfide melt under controlled oxygen and sulfur fugacities. *Geochimica et Cosmochimica Acta* **69**, 4349–4360.

Nordstrom, D. K. & Munoz, J. L. (1994). *Geochemical Thermodynamics*. Hoboken, NY: Blackwell Scientific.

Oudin, E., Marchig, V., Rösch, H., Lalou, C. & Brichet, E. (1990). Observation de CuS_2 à l'état naturel dans une cheminée hydrothermal du Pacific Sud. *Comptes Rendus de l'Académie des Sciences, Série II* **310**, 210–216.

Penniston-Dorland, S. C., Kohn, M. J. & Manning, C. E. (2015). The global range of subduction zone thermal structures from exhumed blueschists and eclogites: Rocks are hotter than models. *Earth and Planetary Science Letters* **428**, 243–254.

Potter, R. & Evans, H. (1976). Definitive X-ray powder data for covellite, annilite, djerlite and chalcocite. *Journal of Research of the US Geological Survey* **4**, 205–212.

Putnis, A. (1977) Electron diffraction study of phase transformations in copper sulfides. *American Mineralogist* **62**, 107–114.

Rice, C. M., Atkin, D., Bowles, J. F. W. & Criddle, A. J. (1979). Nukundamite, a new mineral, and idaite. *Mineralogical Magazine* **43**, 193–200.

Robie, R. A. & Hemingway, B. S. (1995). *Thermodynamic properties of minerals and related substances at 298·15 K and 1 bar pressure and at higher temperature*. US Geological Survey Bulletin **2131**, 461 pp.

Roseboom, E. H. (1966). An investigation of system Cu–S and some natural copper sulfides between 25° and 700 °C. *Economic Geology* **61**, 641–672.

Roseboom, E. H. & Kullerud, G. (1958). The solidus in the system Cu–Fe–S between 400 °C and 800 °C. *Carnegie Institution of Washington, Yearbook* **57**, 222–227.

Schmid-Beurmann, P. & Bente, K. (1995). Stability properties of the CuS_2–FeS_2 solid solution series of pyrite type. *Mineralogy and Petrology* **53**, 333–341.

Schmidt, J. A., Sagua, A. E. & Lescano, E. (1998). Electrochemical investigation of the equilibria (covellite + anilite) and (covellite + digenite). *Journal of Chemical Thermodynamics* **30**, 283–290.

Schoeller, W. R. & Powell, A. R. (1920). Villamaninite, a new mineral. *Mineralogical Magazine* **19**, 14–18.

Schneeberg, E. P. (1973). Sulfur fugacity measurements with the electrochemical cell Ag/AgI/$Ag_{2+x}S$, fS_2. *Economic Geology* **68**, 507–517.

Scott, S. D. (1973). Sphalerite geothermometry and geobarometry. *Economic Geology* **66**, 653–669.

Seal, R. R., Inan, E. E. & Hemingway, B. S. (2001). The Gibbs free energy of nukundamite ($Cu_{3·38}Fe_{0·62}S_4$): a correction and implications for phase equilibria. *Canadian Mineralogist* **39**, 1635–1640.

Shimazaki, H. & Clark, L. A. (1970). Synthetic FeS_2–CuS_2 solid solutions and fukuchilite-like minerals. *Canadian Mineralogist* **10**, 648–664.

Spear, F. S. (1993). *Metamorphic Phase Equilibria and Pressure Temperature–Time Paths*. Chantilly, VA: Mineralogical Society of America.

Sugaki, A., Shima, H., Kitakaze, A. & Harada, H. (1975). Isothermal phase relations in the system Cu–Fe–S under hydrothermal conditions at 350 °C and 300 °C. *Economic Geology* **70**, 806–823.

Sugaki, A., Shima, H., Kitakaze, A. & Mizota, T. (1981). Hydrothermal synthesis of nukundamite and its crystal structure. *American Mineralogist* **66**, 398–402.

Taylor, L. A. & Kullerud, G. (1972). Phase equilibria associated with the stability of copper disulfide. *Neues Jahrbuch für Mineralogie, Monatshefte* **10**, 458–464.

Tenailleau, C., Etschmann, B., Wang, H., Pring, A., Grguric, B. A. & Studer, A. (2005). Thermal expansion of troilite and pyrrhotite determined by *in situ* cooling (873 to 373 K) neutron powder diffraction measurements. *Mineralogical Magazine* **69**, 205–216.

Toulmin, P. & Barton, P. B. (1964). A thermodynamic study of pyrite and pyrrhotite. *Geochimica et Cosmochimica Acta* **28**, 641–671.

Vaughan, D. J. & Craig, J. R. (1997). Sulfide ore mineral stabilities, morphologies, and intergrowth textures. In: Barnes, H. L. (ed.) *Geochemistry of Hydrothermal Ore Deposits*. New York: John Wiley, pp. 367–433.

Wohlgemuth-Ueberwasser, C. C., Fonseca, R. O. C., Ballhaus, C. & Berndt, J. (2013). Sulfide oxidation as a process for the formation of copper-rich magmatic sulfides. *Mineralium Deposita* **48**, 115–127.

Wood, B. J. & Fraser, D. G. (1977). *Elementary Thermodynamics for Geologists*. Oxford: Oxford University Press.

Yund, R. A. & Kullerud, G. (1966). Thermal stability of assemblages in Cu–Fe–S system. *Journal of Petrology* **7**, 454–488.